Dual-Size Silicon Nanocrystal-Embedded SiO_x Nanocomposite as a High-Capacity Lithium Storage Material

Eunjun Park,[†] Hyundong Yoo,[†] Jaewoo Lee,[‡] Min-Sik Park,[*,‡] Young-Jun Kim,[‡] and Hansu Kim[*,†]

[†]Department of Energy Engineering, Hanyang University, 222 Wangsimni-ro, Seongdong-gu, Seoul 133-791, Republic of Korea and [‡]Advanced Batteries Research Center, Korea Electronic Technology Institute, 68 Yatap-dong, Bundang-gu, Seongnam 463-816, Republic of Korea

ABSTRACT SiO_x-based materials attracted a great deal of attention as high-capacity Li^+ storage materials for lithium-ion batteries due to their high reversible capacity and good cycle performance. However, these materials still suffer from low initial Coulombic efficiency as well as high production cost, which are associated with the complicated synthesis process. Here, we propose a dual-size Si nanocrystal-embedded SiO_x nanocomposite as a high-capacity Li^+ storage material prepared *via* cost-effective sol–gel reaction of triethoxysilane with commercially available Si nanoparticles. In the proposed nanocomposite, dual-size Si nanocrystals are incorporated into the amorphous SiO_x matrix, providing a high capacity (1914 mAh g^{-1}) with a notably improved initial efficiency (73.6%) and stable cycle performance over 100 cycles. The highly robust electrochemical and mechanical properties of the dual-size Si nanocrystal-embedded SiO_x nanocomposite presented here are mainly attributed to its peculiar nanoarchitecture. This study represents one of the most promising routes for advancing SiO_x-based Li^+ storage materials for practical use.

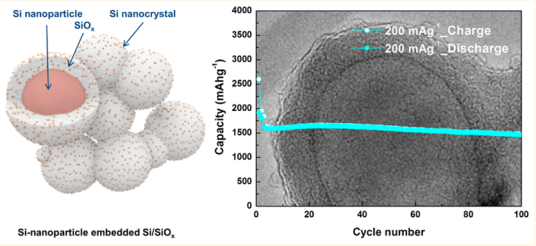

KEYWORDS: lithium-ion battery · Si/SiO_x · Si embedded SiO_x nanocomposites · anodes

The global demand for advanced power sources with a high energy density is increasing due to the rapid growth of emerging markets for various energy storage applications, ranging from portable electronic devices to electric vehicles.[1−4] Although graphite is widely used as an anode material in currently commercialized lithium-ion batteries (LIBs), it does not allow for a further increase in the energy density of LIBs because of its low theoretical capacity (372 mAh g^{-1}, LiC_6).[4−6] To meet the growing demand for high-energy LIBs, the development of high-capacity anode materials is imperative.

Silicon has been considered a promising anode material for replacement of graphite owing to its high theoretical capacity (3580 mAh g^{-1}, $Li_{15}Si_4$) and relatively low redox potential (~0.4 V *vs* Li/Li^+).[6,7] Unfortunately, poor cycle performance of the Si anode, mainly caused by extremely large Si volume changes during alloying/dealloying with Li^+, remains a problem that needs to be resolved before application at a commercial scale.[8−10] To overcome these limitations, various structural modifications of Si have been suggested to effectively control the mechanical strain inevitably produced during cycling.[11−16] In particular, Si/SiO_x nanocomposites, in which the active Si phase is surrounded by an inactive or less active matrix (*i.e.*, the amorphous SiO_x phase), have attracted attention as one of the most promising candidates for commercial use. In this nanocomposite, an amorphous SiO_x matrix acts as a buffer phase against huge Si volume changes during cycling; thus, Si/SiO_x nanocomposites showed better cycle performance and dimensional stability than conventional Si.

Recently, many research groups have proposed various Si/SiO_x nanocomposites as high-capacity Li^+ storage materials. Homma *et al.* developed a SiO_x nanocomposite using plasma spray–physical vapor deposition (PS–PVD) that showed a high reversible capacity of about 1770 mAh g^{-1}

* Address correspondence to parkms@keti.re.kr, khansu@hanyang.ac.kr.

Received for review May 26, 2015 and accepted July 1, 2015.

Published online July 01, 2015
10.1021/acsnano.5b03166

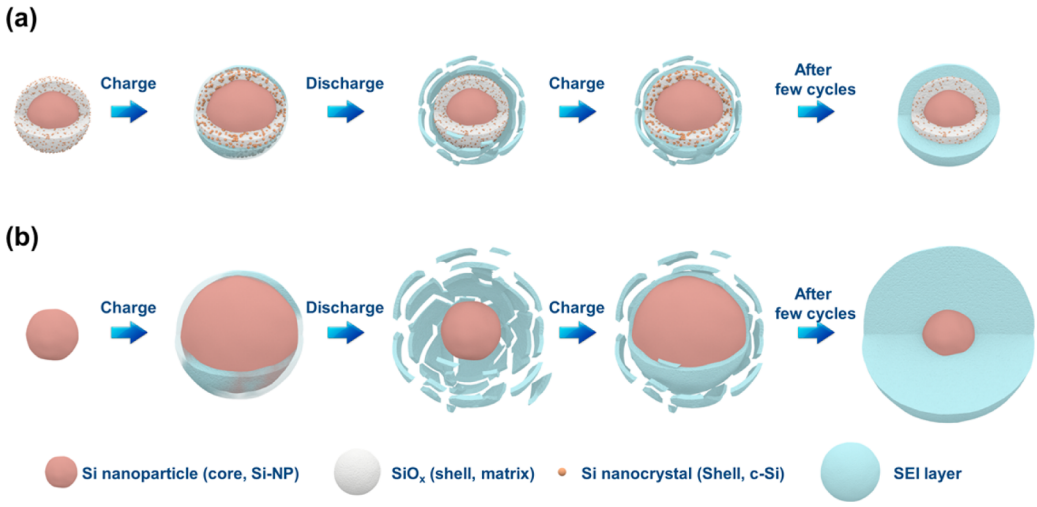

Figure 1. Schematic illustration of (a) SEI formation on the dual-size Si nanocrystal-embedded SiO_x nanocomposite and (b) bare Si nanoparticles during lithiation and delithiation.

with good cycle performance.[17] A Si/SiO_x nanocomposite was also prepared and adopted as a constituent in an anode blended with graphite in some commercial LIBs by another group of researchers.[18] However, the practical use of these materials is still limited by their high production cost, because the fabrication of Si/SiO_x nanocomposites requires both ultrahigh vacuum conditions and temperatures greater than 1400 °C. Recently, we prepared carbon-coated Si nanocrystal (~10 nm)-embedded SiO_x nanospheres with sizes of about 200 nm through a cost-effective sol–gel reaction of triethoxysilane; this material showed a reversible capacity of 950 mAh g^{-1} with excellent capacity retention over 100 cycles.[19] Another attractive feature of this Si/SiO_x nanocomposite is its good dimensional stability during cycling. We found that carbon-coated Si/SiO_x nanosphere electrodes showed height expansion of only 37.5% after 100 cycles. The superior mechanical stability of Si/SiO_x nanocomposites mainly comes from a robust SiO_x matrix phase, which acts as a mechanical buffer to accommodate the tremendous volume changes of Si during cycling. However, its low initial Coulombic efficiency (58%) needs to be further improved because the irreversible capacity loss of the anode in the first cycle causes a decrease in the energy density of the LIB full-cell. The irreversible electrochemical reaction of the SiO_x phase with Li^+ to form lithium silicate (Li–Si–O) in the first cycle is one of the main reasons for the low initial Coulombic efficiency.[20−22] One effective way to raise the initial Coulombic efficiency of the Si/SiO_x nanocomposite is to increase the relative amount of Si in the nanocomposite. However, this can lead to severe degradation in the cycle performance of the Si/SiO_x nanocomposite.

Here, we demonstrate a mechanically robust dual-size Si-embedded SiO_x nanocomposite with a core–shell nanostructure that addresses the aforementioned problems regarding initial Coulombic efficiency and cycle performance. In this core–shell nanostructure, mechanical stress exerted on the more active Si phases during cycling can be effectively mitigated by a surrounding, less-active SiO_x shell layer. The use of a less-active phase in the shell also results in a highly stable solid electrolyte interphase during cycling. Wu *et al.* demonstrated that a double-walled silicon nanotube surrounded by a Li^+-permeable SiO_x layer anode showed highly stable capacity retention over 6000 cycles.[23] More recently, Liu *et al.* prepared a Si/Silicon oxycarbide (Si–O–C) nanocomposite *via* sol–gel reaction of diethoxymethylsilane and triethoxysilane with Si nanoparticles. Despite Si/Si–O–C nanocomposites exhibiting a reversible capacity of 1190 mAh g^{-1} with a high initial efficiency of about 69%, only 76% of this initial capacity was retained after 20 cycles, which is insufficient for commercial use.[24] Choi *et al.* reported that a Si–O–C-coated Si nanoparticle anode showed excellent cycle performance over 200 cycles with a high initial capacity of 2093 mAh g^{-1}.[25] Although these previous reports dealt with different matrix phases (*i.e.*, Si–O–C), they provided insight into the design of our dual-size silicon nanocrystal-embedded SiO_x core–shell nanocomposite. In this work, we focus on compositional and structural modifications of the proposed Si/SiO_x nanocomposite to attain a robust microstructural layout of active and less-active constituents in the nanocomposite, as shown in Figure 1. Furthermore, the proposed material design can be simply synthesized by adding commercially available Si nanoparticles during scalable sol–gel reaction of triethoxysilane in an acidic aqueous medium.

RESULTS AND DISCUSSION

Dual-size Si nanocrystal-embedded Si/SiO_x (denoted as D-Si/SiO_x hereafter) nanocomposites were prepared by simple addition of commercial Si nanoparticles (Si-NPs, <100 nm in size) during a sol–gel reaction of

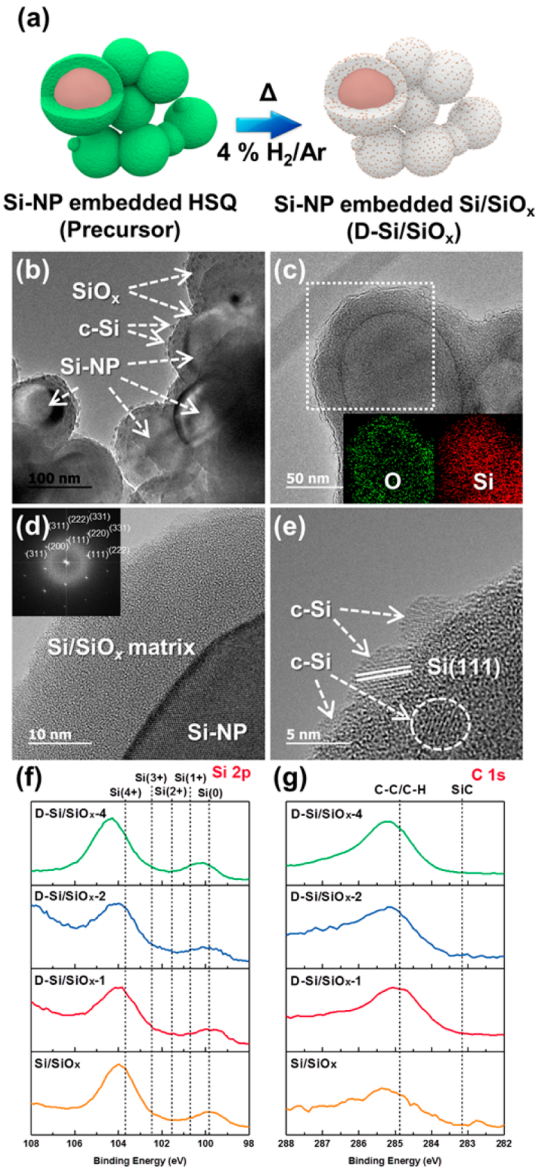

Figure 2. (a) Schematic of D-Si/SiO$_x$ nanocomposite preparation, (b) TEM image of the D-Si/SiO$_x$-1 nanocomposite, (c) TEM image of the D-Si/SiO$_x$-1 nanocomposite combined with EDS elemental mapping results (O, green and Si, red), (d) HRTEM image of D-Si/SiO$_x$-1 nanocomposite, (e) HRTEM image of Si/SiO$_x$ shell of the nanocomposite synthesized by sol−gel reaction. (f) Si 2p and (g) C 1s XPS spectra collected from various D-Si/SiO$_x$ nanocomposites (D-Si/SiO$_x$-1, D-Si/SiO$_x$-2, and D-Si/SiO$_x$-4).

triethoxysilane followed by heat treatment at 1000 °C, as illustrated in Figure 2a. Various D-Si/SiO$_x$ nanocomposites with different amounts of Si-NPs were obtained; the weight ratios of Si-NP to $HSiO_{1.5}$ were fixed at 1, 2, and 4 in this work. Morphologies of D-Si/SiO$_x$ nanocomposites with different amounts of Si-NPs were characterized using FESEM. All nanocomposites have a similar spherical particle shape with an average particle size of 300−500 nm (Supporting Information Figure S1). This size is larger than Si/SiO$_x$ nanocomposites without Si-NPs (Supporting Information Figure S2) and commercial Si-NPs (Supporting Information Figure S3).

Microstructures of D-Si/SiO$_x$ nanocomposites were further investigated using TEM. As-prepared D-Si/SiO$_x$ nanocomposites had a typical core−shell structure, in which crystalline Si-NPs (<100 nm) are uniformly covered with a Si/SiO$_x$ matrix (Figure 2b,c). EDS elemental mapping results revealed that a higher oxygen content was detected in the Si/SiO$_x$ shell rather than the Si-NP core (inset of Figure 2c). The thickness of the Si/SiO$_x$ shell was measured to be about 20−30 nm (Figure 2d). We also found that many smaller Si nanocrystals with sizes of about 5 nm were incorporated into the SiO$_x$ shell, as shown in Figure 2e. These smaller Si nanocrystals were mainly formed as a result of the thermal decomposition of $HSiO_{1.5}$ at 1000 °C under a reducing atmosphere.[26−28]

Further structural characterization of these materials was carried out using powder XRD and XPS. XRD patterns of D-Si/SiO$_x$ nanocomposites with different amounts of Si-NP showed a broad Bragg peak at 2θ = 21.8°, which was attributed to the amorphous SiO$_x$ matrix of the Si/SiO$_x$ shell (Supporting Information Figure S4). Reflections appearing at 2θ = 28.6, 47.6, 56.5, 69.7, and 77.0° matched the Bragg peaks of crystalline Si. The growth of these peaks was evidenced by increasing Si-NP content in the nanocomposites. Peaks associated with smaller Si nanocrystals (less than 10 nm) embedded in the SiO$_x$ matrix were not detectable in the XRD pattern of the Si/SiO$_x$ nanocomposite even though they were clearly found in the TEM images (Figure 2e). This can be explained by the fact that the Si nanocrystals dispersed in the amorphous SiO$_x$ matrix have a short-range crystalline order,[26] which is not detectable in XRD analysis. Smaller Si nanocrystals in the Si/SiO$_x$ nanocomposites were characterized by XPS analysis. Figure 2f shows Si 2p XPS spectra of D-Si/SiO$_x$ nanocomposites and a Si/SiO$_x$ nanocomposite without Si-NPs. Even though Si-NPs were not added in the Si/SiO$_x$ nanocomposite, a peak corresponding to elemental Si (~99.5 eV) was clearly observed, indicating the presence of smaller Si nanocrystals, as confirmed by TEM observations. Furthermore, it should be noted that there is no evidence for Si−C bonds in the D-Si/SiO$_x$ or the Si/SiO$_x$ nanocomposite (Figure 2g) even after Ar^+ sputtering for 300 s (Supporting Information Figures S5 and S6), implying that the SiO$_x$ matrix consists only of silicon and oxygen.

Figure 3a shows voltage profiles of D-Si/SiO$_x$ nanocomposite anodes during the first cycle. Cells were charged (Li^+ insertion) and discharged (Li^+ extraction) in a voltage range from 0.01 to 2.0 V *vs* Li/Li^+ at a constant current density of 0.2 C (200 mA g^{-1}). The initial reversible capacities of the anodes were 1914 mAh g^{-1} (D-Si/SiO$_x$-1), 1536 mAh g^{-1} (D-Si/SiO$_x$-2), and 1352 mAh g^{-1} (D-Si/SiO$_x$-4). The introduction of Si-NPs increased the discharge capacity of the D-Si/SiO$_x$ nanocomposite by expanding the voltage plateau at around 0.4 V *vs* Li/Li^+. This plateau corresponded to the redox

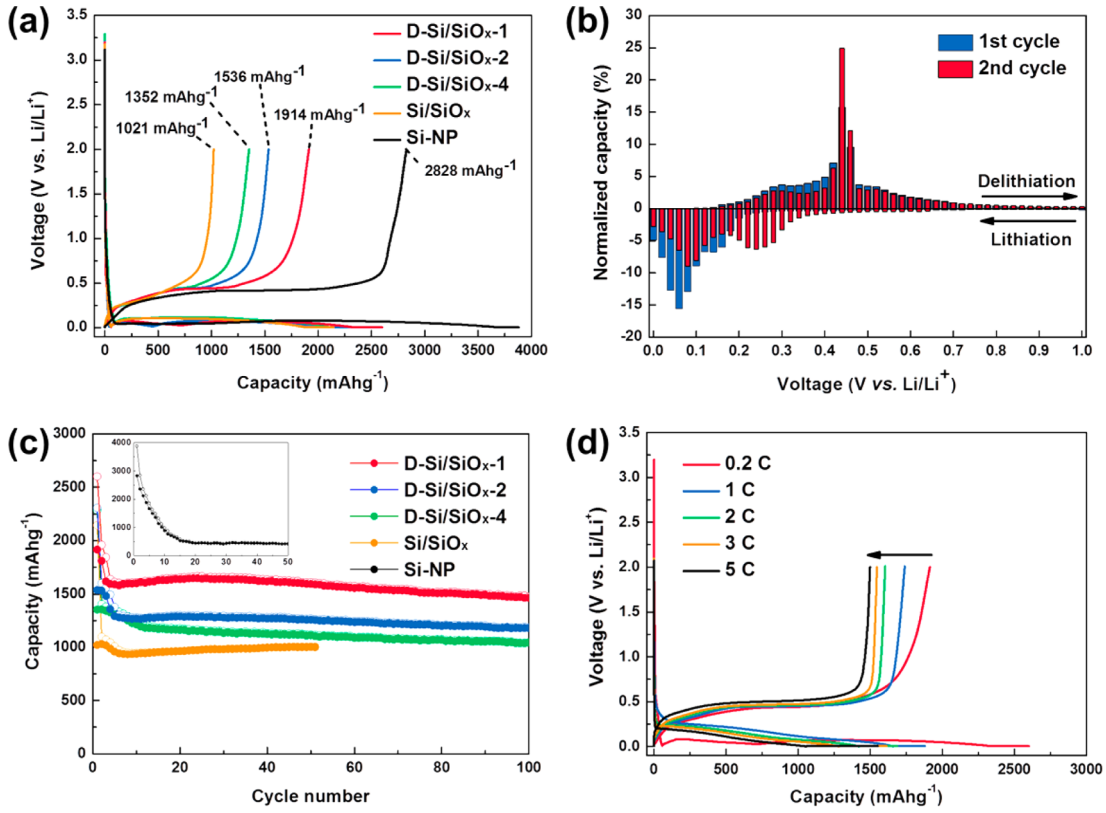

Figure 3. (a) Galvanostatic voltage profiles of D-Si/SiO$_x$-1 nanocomposite anodes in a voltage range of 0.01−2.0 V *vs* Li/Li$^+$ at a constant current density of 0.2 C (200 mA g^{-1}) in the first cycle, (b) PITT profiles of the D-Si/SiO$_x$-1 nanocomposite anode recorded by a potential step of 10 mV in the first and second cycles, (c) cycle performance of D-Si/SiO$_x$ nanocomposite anodes at a constant current of 0.2 C (200 mA g^{-1}) for 100 cycles, (d) rate-capability of D-Si/SiO$_x$ nanocomposite anodes at different current densities of 0.5, 1.0, 2.0, 3.0, and 5.0 C (1 C = 1000 mA g^{-1}).

potential of dealloying the Li$_x$Si phase during discharge. These results reveal that Si-NPs in the nanocomposites are mainly responsible for the notable increase in the reversible capacity of D-Si/SiO$_x$ nanocomposites. Furthermore, the addition of Si-NPs also increased the initial Coulombic efficiencies of D-Si/SiO$_x$ nanocomposites, which were measured to be 73.6% for D-Si/SiO$_x$-1, 66.7% for D-Si/SiO$_x$-2, and 59.2% for D-Si/SiO$_x$-4, respectively. These values are much higher than those of Si/SiO$_x$ nanospheres (47.6%). Based on these results, we conclude that the introduction of Si-NPs into the Si/SiO$_x$ nanocomposite is quite effective in improving the reversible capacity and initial Coulombic efficiency simultaneously.

Figure 3b shows potentiostatic intermittent titration technique (PITT) profiles collected from the D-Si/SiO$_x$-1 nanocomposite anode during the two initial cycles. From the results, we confirmed that lithiation and delithiation of the D-Si/SiO$_x$-1 nanocomposite mainly occur at 0.25 and 0.45 V *vs* Li/Li$^+$, respectively, in the second cycle. This suggests that the electrochemical performance of the D-Si/SiO$_x$-1 nanocomposite might mainly be governed by embedded Si-NPs.

Figure 3c,d shows the cycle performance and rate capability of the D-Si/SiO$_x$ nanocomposite anodes, respectively. All D-Si/SiO$_x$ nanocomposite anodes exhibited stable cycle performance up to 100 cycles without the significant capacity fading generally observed in the commercial Si anode (Figure 3c). In particular, the D-Si/SiO$_x$-1 nanocomposite anode retained a high discharge capacity of more than 1500 mAh g^{-1} even after 100 cycles. The D-Si/SiO$_x$-2 and D-Si/SiO$_x$-4 nanocomposite anodes also exhibited excellent cyclic retention up to 100 cycles, regardless of Si-NP content. This indicates that the dual-size Si nanocrystal-embedded core−shell nanoarchitecture proposed here would be advantageous for accommodating severe volume changes in the active Si phase by integrating a less-active SiO$_x$ shell. The SiO$_x$ shell effectively reduced mechanical strain due to the dimensional changes of Si-NPs during cycling. The shell also ensured the formation of a highly stable SEI film on the surface of the nanocomposite against repeated volume expansion and contraction of more active Si phases in the nanocomposite. Thus, excellent cycle performance as well as high reversible capacity can be simultaneously attained without significant capacity loss during cycling. The reversible capacity of the proposed core−shell nanocomposite material can be easily tailored by adjusting the amount of Si-NPs. Note that our material design does not require the additional carbon coating usually used to improve the electrochemical performance of

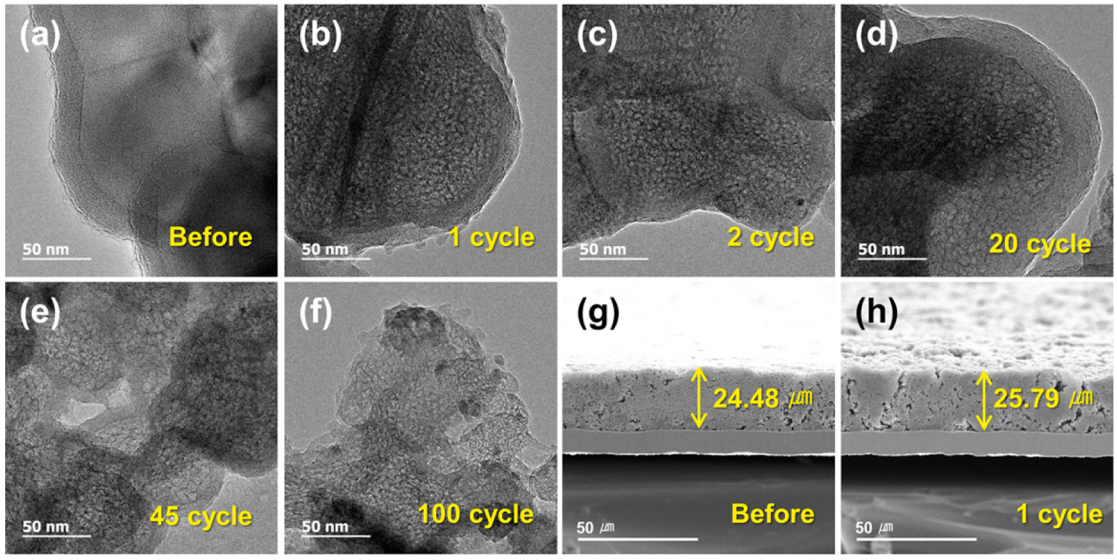

Figure 4. TEM observations of D-Si/SiO_x-1 nanocomposite collected at different cycles: (a) pristine (before cycling), (b) after 1 cycle, (c) after 2 cycles, (d) after 20 cycles, (e) after 45 cycles, and (f) after 100 cycles. Cross-sectional FESEM images of the D-Si/SiO_x-1 nanocomposite anode at different cycles: (g) pristine (before cycling), (h) after 1 cycle.

SiO_x-based anode materials, thus enabling further reduction of production cost.[29,30]

The structural stability of D-Si/SiO_x nanocomposites was investigated by post-mortem analyses of the structure. Figure 4 clearly shows structural changes of the D-Si/SiO_x-1 nanocomposite characterized by *ex situ* TEM analyses during cycling. The D-Si/SiO_x-1 nanocomposite has a typical core−shell structure before cycling (Figure 4a). Conversion of crystalline Si-NPs to a porous structure was obvious even after 1 cycle (Figure 4b). Interestingly, in contrast to Si-NPs, no structural changes were observed in the Si/SiO_x shell of the nanocomposite. The core−shell structured D-Si/SiO_x-1 nanocomposite still maintained its initial morphology up to 45 cycles (Figure 4c−e), implying that the Si/SiO_x shell is capable of accommodating severe volume expansion of the Si-NP core. After 100 cycles, however, a partial collapse of the core−shell structure of the D-Si/SiO_x-1 nanocomposite was observed, as shown in Figure 4f. Furthermore, the dimensional stability of the D-Si/SiO_x-1 nanocomposite anode was also investigated in this work. Figure 4g shows a cross-sectional FESEM image of a pristine D-Si/SiO_x-1 nanocomposite anode before cycling; therein, the thickness of the anode was measured to be 24.5 μm. After 1 cycle, the anode expanded to a thickness of 25.8 μm, indicating a 5.3% dimensional change (Figure 4h). Note that the active materials remained intact without notable microcrack formation or further pulverization even after 100 cycles (Supporting Information Figure S7).

To further improve the battery performance of D-Si/SiO_x nanocomposites, an additional carbon coating layer was added to the surface of D-Si/SiO_x materials with coal-tar pitch as a carbon precursor, as shown in Figure 5a,b. FESEM and TEM observations showed a conformal carbon coating layer on the surface of the D-Si/SiO_x nanocomposites. From the TGA curve (Supporting Information Figure S8), we confirmed the carbon content (22.3 wt %) in the C-coated D-Si/SiO_x-1 nanocomposite. Panels c and d of Figure 5 show the electrochemical voltage profiles for the first cycle and the cycle performance of C-coated D-Si/SiO_x nanocomposite anode materials, respectively. Although the reversible capacity decreased due to carbon coating, capacity retention improved during cycling. In particular, capacity fading in the first few cycles of the D-Si/SiO_x nanocomposites (Figure 3c) was clearly reduced by the additional carbon coating layer, resulting in more stable capacity retention over 100 cycles. It is noticeable that surface carbon layer is effective for ensuring sufficient electrical conduction, leading to stable cycle performance. Overall, we strongly emphasize that the Si/SiO_x shell plays an important role as a buffer phase against mechanical strain induced by the huge volume change of Si-NPs during cycling; this results in outstanding cycle performance of the D-Si/SiO_x nanocomposites anodes.

CONCLUSIONS

We demonstrated a cost-effective sol−gel synthesis route for Si/SiO_x nanocomposites with a core−shell structure in which dual-size crystalline Si approximately 50 nm and less than 10 nm in size are incorporated as active materials into an amorphous SiO_x matrix. This mechanically robust design of D-Si/SiO_x nanocomposites provided highly efficient Li^+ storage and dimensional stability. In particular, the D-Si/SiO_x-1 nanocomposite anode exhibited a high reversible capacity of more than 1500 mAh g^{-1} with an initial Coulombic efficiency of 73.6% and excellent cycle

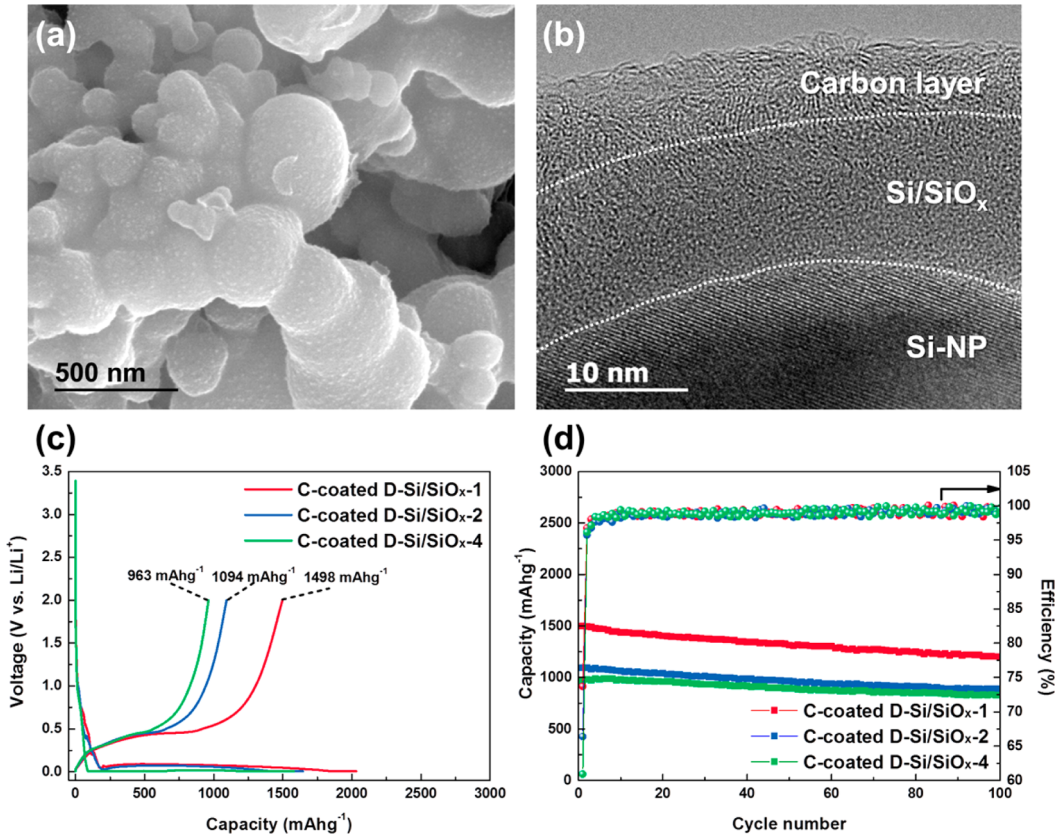

Figure 5. (a) FESEM image and (b) HRTEM image of the C-coated D-Si/SiO_x-1 nanocomposite, and (c) galvanostatic voltage profiles of C-coated D-Si/SiO_x nanocomposite anodes in a voltage range of 0.01−2.0 V *vs* Li/Li^+ at a constant current density of 0.2 C (200 mA g^{-1}) during the first cycle, (d) cycle performance of C-coated D-Si/SiO_x nanocomposite anodes at a constant current 0.2 C (200 mA g^{-1}) for 100 cycles.

performance up to 100 cycles. The outstanding cycle performance of the proposed nanocomposite was mainly attributed to the SiO_x shell in the nanocomposite, which acts as a buffer phase to accommodate volume change of the crystalline Si without significant degradation. This approach provides a means of improving the electrochemical properties of Si-based anode materials for use in commercial LIBs.

METHODS

Material Preparation. To prepare Si nanocrystal-embedded HSQ (hydrogen silsesquioxane, $HSiO_{1.5}$) precursors, different quantities of commercial Si nanopowders (Nanostructured & Amorphous Materials, Inc.) with a size of 50−100 nm were dispersed in 0.1 M HCl solution (25 mL). The mass ratio of HSQ to Si nanopowder was varied to be 1:1, 2:1, and 4:1. Subsequently, 2.5 mL of triethoxysilane ($(C_2H_5O)_3SiH$; Aldrich, 99.8%) was added to the solution under stirring at 500 rpm for 20 min. The solution was filtered and washed with deionized water repeatedly. The filtered powders were carefully gathered and dried in a vacuum oven at 110 °C for 6 h to remove any residual water. Dual-size Si nanocrystal-embedded Si/SiO_x nanocomposites with varying Si content were obtained by heat treatment at 1000 °C for 1 h under a 4% H_2/Ar atmosphere with a flow rate of 0.5 l min^{-1}. The heating rate was fixed at 20 °C min^{-1}. To obtain a uniform carbon coating, the dual-size Si nanocrystal-embedded Si/SiO_x nanocomposites were ground with coal-tar pitch at a weight ratio of 7:3. The mixture was carefully poured into a tetrahydrofuran (THF) solution (200 mL) under constant stirring at 200 rpm at 50 °C. After the solvent evaporated, the product was collected and loaded into a vertical furnace and was heated to 1000 °C for 2 h under a N_2 atmosphere. Finally, the C-coated dual-size Si nanocrystal-embedded Si/SiO_x nanocomposites were ground again before use.

Structural Characterization. The morphology and microstructure of the dual-size Si nanocrystal-embedded Si/SiO_x nanocomposites were characterized using a field-emission scanning electron microscope (FESEM; JEOL JSM-7000F) and a high-resolution transmission electron microscope (HRTEM; JEOL ARM-200F). The microstructure was further identified by conducting powder X-ray diffraction (XRD) with an X-ray diffractometer (Empyrean, PANanalytical). A Raman spectrometer (Bruker Senterra Grating 400) with a He−Ne laser at a wavelength of 532 nm was also used to study microstructure. The surface chemistry of the proposed nanocomposites was investigated using X-ray photoelectron spectroscopy (XPS, Thermo Scientific Sigma Probe).

Electrochemical Measurements. A slurry was made consisting of active material powder (70 wt %) with a mass of 1.5 mg cm^{-2}, conductive agent (Super-P, 15 wt %) and poly(acrylic acid) binder (PAA, 15 wt %) dissolved in deionized water. Electrodes were prepared by placing this slurry on the Cu foil substrate. After coating, the electrodes were dried at 120 °C for 12 h under vacuum and were pressed under a pressure of 200 kg cm^{-2}. A coin-type (CR2032) half-cell was assembled with Li metal as a counter and reference electrode in a dry room using a polyethylene (PE) membrane as a separator. Then, 1 M $LiPF_6$ dissolved in a mixed solvent of ethylene carbonate (EC) and diethyl carbonate (DEC) (3:7, v/v; Panax Etec Co. Ltd.) was used

as an electrolyte. The cells were tested in constant current−constant voltage (CC−CV) mode in a voltage window of 0.01−2.0 V *vs* Li/Li^+ at room temperature.

Conflict of Interest: The authors declare no competing financial interest.

Acknowledgment. This research was supported in part by the R&D Center for Valuable Recycling (Global-Top Environmental Technology Development Program, No. GT-11-C-01-080-0), funded by the Ministry of Environment, Korea, and by the Korea Institute of Energy Technology Evaluation and Planning (KETEP), which is funded by the Ministry of Trade, Industry & Energy, Republic of Korea (No. 20128510010080).

Supporting Information Available: Figures showing FESEM images, XRD patterns and XPS spectra. The Supporting Information is available free of charge on the ACS Publications website at DOI: 10.1021/acsnano.5b03166.

REFERENCES AND NOTES

1. Armand, M.; Tarascon, J.-M. Building Better Batteries. *Nature* **2008**, *451*, 652–657.
2. Pramanik, M.; Tsujimoto, Y.; Malgras, V.; Dou, S. X.; Kim, J. H.; Yamauchi, Y. Mesoporous Iron Phosphonate Electrodes with Crystalline Frameworks for Lithium-Ion Batteries. *Chem. Mater.* **2015**, *27*, 1082–1089.
3. Hwang, S. M.; Lim, Y.-G.; Kim, J.-G.; Heo, Y. -U; Lim, J. H.; Yamauchi, Y.; Park, M.-S.; Kim, Y.-J.; Dou, S. X.; Kim, J. H. A Case Study on Fibrous Porous SnO_2 Anode for Robust, High-Capacity Lithium-Ion Batteries. *Nano Energy* **2014**, *10*, 53–62.
4. Jeong, G.; Kim, Y.-U.; Kim, H.; Kim, Y.-J.; Sohn, H.-J. Prospective Materials and Applications for Li Secondary Batteries. *Energy Environ. Sci.* **2011**, *4*, 1986–2002.
5. Palacín, M. R. Recent Advances in Rechargeable Battery Materials: A Chemist's Perspective. *Chem. Soc. Rev.* **2009**, *38*, 2565–2575.
6. Hatchard, T. D.; Dahn, J. R. *In Situ* XRD and Electrochemical Study of the Reaction of Lithium with Amorphous Silicon. *J. Electrochem. Soc.* **2004**, *151*, A838–A842.
7. Netz, A.; Huggins, R. A.; Weppner, W. The Formation and Properties of Amorphous Silicon as Negative Electrode Reactant in Lithium Systems. *J. Power Sources* **2003**, *119−121*, 95–100.
8. Beaulieu, L. Y.; Eberman, K. W.; Turner, R. L.; Krause, L. J.; Dahn, J. R. Colossal Reversible Volume Changes in Lithium Alloys. *Electrochem. Solid-State Lett.* **2001**, *4*, A137–A140.
9. Huggins, R. A.; Nix, W. D. Decrepitation Model for Capacity Loss During Cycling of Alloys in Rechargeable Electrochemical Systems. *Ionics* **2000**, *6*, 57–63.
10. Obrovac, M. N.; Krause, L. J. Reversible Cycling of Crystalline Silicon Powder. *J. Electrochem. Soc.* **2007**, *154*, A103–A108.
11. Magasinski, A.; Dixon, P.; Hertzberg, B.; Kvit, A.; Ayala, J.; Yushin, G. High-Performance Lithium-Ion Anodes Using a Hierarchical Bottom-Up Approach. *Nat. Mater.* **2010**, *9*, 353–358.
12. Kasavajjula, U.; Wang, C.; Appleby, A. J. Nano- and Bulk-Silicon-Based Insertion Anodes for Lithium-Ion Secondary Cells. *J. Power Sources* **2007**, *163*, 1003–1039.
13. Chan, C. K.; Peng, H.; Liu, G.; McIlwrath, K.; Zhang, X. F.; Huggins, R. A.; Cui, Y. High-Performance Lithium Battery Anodes Using Silicon Nanowires. *Nat. Nanotechnol.* **2008**, *3*, 31–35.
14. Kim, H.; Cho, J. Superior Lithium Electroactive Mesoporous Si@Carbon Core-Shell Nanowires for Lithium Battery Anode Material. *Nano Lett.* **2008**, *8*, 3688–3691.
15. Song, T.; Xia, J.; Lee, J.-H.; Lee, D. H.; Kwon, M.-S.; Choi, J.-M.; Wu, J.; Doo, S. K.; Chang, H.; Park, W. I.; et al. Arrays of Sealed Silicon Nanotubes as Anodes for Lithium Ion Batteries. *Nano Lett.* **2010**, *10*, 1710–1716.
16. Yao, Y.; McDowell, M. T.; Ryu, I.; Wu, H.; Liu, N.; Hu, L.; Nix, W. D.; Cui, Y. Interconnected Silicon Hollow Nanospheres for Lithium-Ion Battery Anodes with Long Cycle Life. *Nano Lett.* **2011**, *11*, 2949–2954.
17. Homma, K.; Kambara, M.; Yoshida, T. High Throughput Production of Nanocomposite SiO_x Powders by Plasma Spray Physical Vapor Deposition for Negative Electrode of Lithium Ion Batteries. *Sci. Technol. Adv. Mater.* **2014**, *15*, 025006.
18. Yamada, M.; Ueda, A.; Matsumoto, K.; Ohzuku, T. Silicon-Based Negative Electrode for High-Capacity Lithium-Ion Batteries: "SiO"-Carbon Composite. *J. Electrochem. Soc.* **2011**, *158*, A417–A421.
19. Park, M.-S.; Park, E.; Lee, J.; Jeong, G.; Kim, K. J.; Kim, J. H.; Kim, Y.-J.; Kim, H. Hydrogen Silsequioxane-Derived Si/SiO_x Nanospheres for High-Capacity Lithium Storage Materials. *ACS Appl. Mater. Interfaces* **2014**, *6*, 9608–9613.
20. Miyachi, M.; Yamamoto, H.; Kawai, H.; Ohta, T.; Shirakata, M. Analysis of SiO Anodes for Lithium-Ion Batteries. *J. Electrochem. Soc.* **2005**, *152*, A2089–A2091.
21. Philippe, B.; Dedryvère, R.; Allouche, J.; Lindgren, F.; Gorgoi, M.; Rensmo, H.; Gonbeau, D.; Edström, K. Nanosilicon Electrodes for Lithium-Ion Batteries: Interfacial Mechanisms Studied by Hard and Soft X-Ray Photoelectron Spectroscopy. *Chem. Mater.* **2012**, *24*, 1107–1115.
22. Lee, J. K.; Kim, B. K.; Yoon, W. Y. Irreversible Behaviors and Kinetics of Lithiated Products in SiO_x Anodes with Inserting Li Contents in Li Ion Batteries. *Jpn. J. Appl. Phys.* **2013**, *52*, 10MB10.
23. Wu, H.; Chan, G.; Choi, J. W.; Ryu, I.; Yao, Y.; McDowell, M. T.; Lee, S. W.; Jackson, A.; Yang, Y.; Hu, L.; et al. Stable Cycling of Double-Walled Silicon Nanotube Battery Anodes Through Solid-Electrolyte Interphase Control. *Nat. Nanotechnol.* **2012**, *7*, 310–315.
24. Liu, X.; Xie, K.; Zheng, C.-M.; Wang, J.; Jing, Z. Si-O-C Materials Prepared with a Sol-Gel Method for Negative Electrode of Lithium Battery. *J. Power Sources* **2012**, *214*, 119–123.
25. Choi, S.; Jung, D. S.; Choi, J. W. Scalable Fracture-Free SiOC Glass Coating for Robust Silicon Nanoparticle Anodes in Lithium Secondary Batteries. *Nano Lett.* **2014**, *14*, 7120–7125.
26. Xie, Z.; Henderson, E. J.; Dag, Ö.; Wang, W.; Lofgreen, J. E.; Kübel, C.; Scherer, T.; Brodersen, P. M.; Gu, Z.-Z.; Ozin, G. A. Periodic Mesoporous Hydridosilica-Synthesis of an "Impossible" Material and Its Thermal Transformation into Brightly Photoluminescent Periodic Mesoporous Nanocrystal Silicon-Silica Composite. *J. Am. Chem. Soc.* **2011**, *133*, 5094–5102.
27. Hessel, C. M.; Henderson, E. J.; Veinot, J. G. C. An Investigation of the Formation and Growth of Oxide-Embedded Silicon Nanocrystals in Hydrogen Silsesquioxane-Derived Nanocomposites. *J. Phys. Chem. C* **2007**, *111*, 6956–6961.
28. Hessel, C. M.; Henderson, E. J.; Veinot, J. G. C. Hydrogen Silsesquioxane: A Molecular Precursor for Nanocrystalline $Si-SiO_2$ Composites and Freestanding Hydride-Surface-Terminated Silicon Nanoparticles. *Chem. Mater.* **2006**, *18*, 6139–6146.
29. Tao, H.-C.; Huang, M.; Fan, L.-Z.; Qu, X. Interweaved $Si@SiO_x/C$ Nanoporous Spheres as Anode Materials for Li-Ion Batteries. *Solid State Ionics* **2012**, *220*, 1–6.
30. Wang, J.; Zhao, H.; He, J.; Wang, C.; Wang, J. Nano-sized SiO_x/C Composite Anode for Lithium Ion Batteries. *J. Power Sources* **2011**, *196*, 4811–4815.